Landé *g* Tensor in Semiconductor Nanostructures

T. P. Mayer Alegre,[1,2] F. G. G. Hernández,[1,2] A. L. C. Pereira,[1] and G. Medeiros-Ribeiro[1,*]

[1]*Laboratório Nacional de Luz Síncrotron, Caixa Postal 6192, CEP 13084-971, Campinas, SP, Brazil*
[2]*Instituto de Física Gleb Wataghin Universidade Estadual de Campinas, Campinas, SP, Brazil*

Understanding the electronic structure of semiconductor nanostructures is not complete without a detailed description of their corresponding spin-related properties. Here we explore the response of the shell structure of InAs self-assembled quantum dots to magnetic fields oriented in several directions, allowing mapping of the *g*-tensor modulus for the *s* and *p* shells. We find that the *g* tensors for the *s* and *p* shells exhibit a very different behavior. The *s* state, being more localized, probes the confinement potential details by sweeping the magnetic-field orientation from the growth direction towards the in-plane direction. For the *p* state, the *g*-tensor modulus is closer to that of the surrounding GaAs, consistent with a larger delocalization. In addition to the assessment of the *g* tensor, these results reveal further details of the confining potentials of self-assembled quantum dots that have not yet been probed.

Electronic magnetism in semiconductor nanostructures is one of the important properties to be harnessed in spintronic devices [1] as well as in prototypical systems for quantum information processing [2]. In order to understand and separate the effects of quantum confinement and band structure, including spin-orbit coupling, strain, and nonparabolicity effects, the response of the electronic spin on an applied static magnetic field can provide an improved picture of the overall quantum system. The electronic *g* tensor, which describes the symmetries and magnetic response of the unpaired electron system, is thus a very important tool to assess and investigate these fundamental aspects of spin electronics in nanostructures.

For conduction electrons in bulk semiconductor crystals, the *g* factor can be determined accurately by second-order **k · p** theory using Roth's equation [3,4] and confirmed by experiment [5]. For unpaired electrons bound to donors, *g*-tensor differences from the free atom value of 2 for the ground state will reveal the dependence on the crystal field and spin-orbit coupling [6]. The symmetries of defects and chemical environment can be also revealed by mapping the *g* tensor [7]. In addition to that, the anisotropic part of *g* influences spin-lattice relaxation and is important for spin-related applications [8,9]. For the case of quantum wells [10] and wires [11], the *g* tensor will be affected by quantum confinement, strain, and composition fluctuations.

Experimental investigations of *g* factors and *g* tensors have been reported for metallic nanoparticles [12] and lithographically defined quantum dots (QDs) [13,14]. For metallic nanoparticles, the difficulties arise in finding the symmetry axis, which can be determined from the *g*-tensor mapping. In addition, because the electron mean free path is smaller than the particle size, angular momentum may not be a good quantum number. For lithographically defined quantum dots, the Zeeman splitting and the orbital splitting have comparable energy scales, thus preventing

the evaluation of the out-of-plane *g*-tensor component. For self-assembled quantum dots, a number of experiments have demonstrated striking similarities with the atomic behavior, such as Hund's rules and the Aufbau principle in determining the shell filling for electrons [15,16]. The charging, Zeeman splitting, and single-particle energies are all different for this case, which allows them to be distinguished for excitons and electrons [17–20]. More recently, calculations were carried out displaying the relationship between the *g* tensor and the electronic structure for quantum dots [21].

In this Letter, we explore the shell-structure-dependent spin properties of electrons trapped in InAs QDs. By evaluating the electron addition energies inferred from magnetocapacitance data, we present an experimental account on the *g*-tensor modulus for the *s* and *p* states which were mapped out according to the crystallographic directions of highest symmetry.

InAs QDs were grown by molecular beam epitaxy and capped with thin InGaAs strain reducing layers, as described elsewhere [19,20]. These structures were embedded in capacitance structures that were subsequently defined by conventional photolithography. The area of the devices was 4×10^{-2} mm^2, hence encompassing an ensemble of about 10^8 QDs per device. Magnetocapacitance experiments were carried out at 2.7 K for magnetic-field intensities ranging from 0 to 15 T. Field sweeps were performed at 15° intervals covering at least 180° by tilting the sample with a goniometer.

Figure 1(a) shows the second derivative of magnetocapacitance spectra taken for field sweeps along the [001] and [110] directions (polar scan). The energy scale derived from the applied bias and voltage-dependent lever arm is translated into the chemical potential within the QDs referenced to the GaAs conduction-band edge. The lever arm was calculated taking into account depletion effects in the back contact [20], thus allowing the determi-
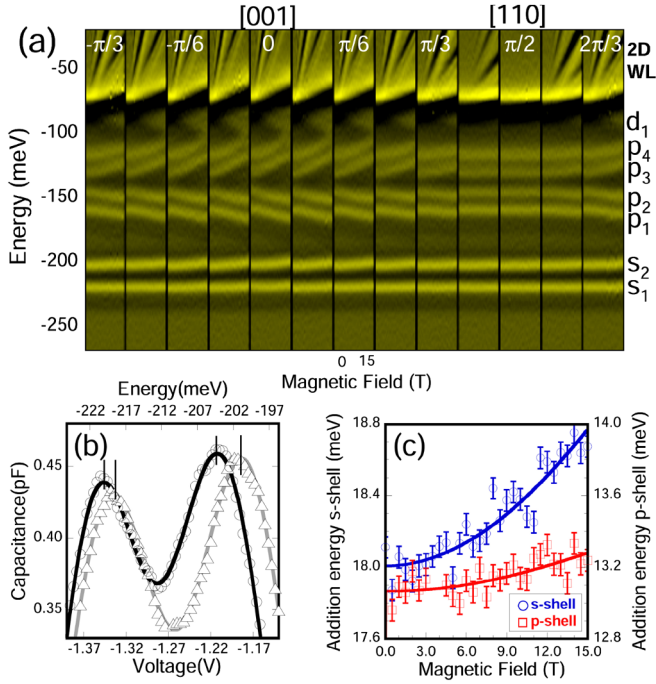
FIG. 1 (color online). (a) Measured data (derivative) for the polar scan, i.e., the magnetic field sweeping from parallel to the [001] direction towards the [110] direction. The gray scale is keyed to the second derivative of the capacitance spectra, with light colors indicating a higher density of states. Each of the 13 frames corresponds to B sweeps from 0 to 15 T, taken at 15° intervals with θ the angle between B and [001]. The s, p, and d states, as well as the wetting layer 2D levels are indicated also. (b) Different capacitance spectra showing the filling of the s shell with 1 and 2 electrons, dots correspond to $\mathbf{B} = 0$ T and triangles to $|\mathbf{B}| = 15$ T, and $\theta = \pi/12$. The solid lines correspond to two Gaussian fits. (c) Fits to Eq. (1) for s and p shell electron addition energies for $\theta = \pi/2$.

nation of a precise energy scale. The gray scale map is a representation of the density of states, where the 0D (up to ~ -80 meV) and 2D (above ~ -80 meV) levels associated with the QDs and wetting layer can be easily identified. For an in-plane field, all orbital effects are minimized given the pancake geometry of the quantum dots; also negligible are the effects of the magnetic field on the wetting layer, which exhibits Landau-level fillings for magnetic fields perpendicular to the sample surface.

From the electron addition energies [16,19,20], orbital, electrostatic, and Zeeman contributions can be separated. Figure 1(b) shows the shift of the capacitance peaks for the sequential charging of the s level on the applied magnetic field for $\theta = \pi/12$. The effects of Coulomb charging, diamagnetic shifts, and Zeeman splitting can be seen in these data. One can separate the orbital effect contribution from the others by subtracting the peak positions, as the diamagnetic contribution is the same for both. For the s shell, using a Fock-Darwin (FD) formalism [15,20], one has for the loading of the first and second electrons for $T = 0$ and $B \parallel [001]$: $E_{s1} = E_z + \hbar\Omega - |g_{zz}|\beta B/2$ and $E_{s2} =$

$E_{s1} + |g_{zz}|\beta B + E_C^s$, where E_z is the confinement along the growth direction, $\Omega = \sqrt{\omega_0^2 + \omega_c^2/4}$, with ω_c as the cyclotron frequency, E_C^s the Coulomb charging energy at zero magnetic field for the s shell electrons, and $|g_{zz}|\beta B$ the Zeeman splitting. For the s shell, one finds $\hbar\omega_0 = 37.8 \pm 0.2$ meV and $E_z \sim -280$ meV. Detailed modeling can provide an even better description [16]; however, it is not necessary to capture the essential features. Electrostatic effects can be calculated given the single-particle energies within the FD framework [15]. For the s and p shells, we find $E_{ss} = 17.2$ meV and $E_{pp} = 13.4$ meV. Figure 1(c) shows the dependence of the addition energies for the s-s and p-p configurations on the applied magnetic field for $\theta = \pi/2$. We find that an agreement within 5%–15% can be found from the calculated and measured addition spectra.

Two effects must be considered when analyzing these data—(i) wave function compression and its effect on the charging energies and (ii) temperature. As the magnetic field is raised, the wave function is compressed which increases the Coulomb charging energies. Under the FD formalism, this effect can be calculated as $E_C^i(B) = E_C^i(0)(1 + \omega_c^2/4\omega_0^2)^{1/4}$, where $E_C^i(0)$ is the Coulomb charging energy at zero magnetic field for the i shell. This effect takes place for all directions of the applied magnetic field but to a lesser extent for the in-plane configuration due to a stronger confinement along the growth direction. As a zeroth-order approximation, we assume this effect to be the same for all configurations. The consequence of this assumption is to underestimate the Zeeman contribution for in-plane magnetic fields.

As stated above, the experiments were carried out with QD ensembles. Thus, an accurate description of this system at finite temperatures requires usage of a magnetization model for a system of n noninteracting spins, which can be carried out by calculating the partition function for the system. For the current analysis, we take into account the temperature-dependent spin contribution on the addition energy spectra. This yields a direct relationship between the addition energy $\Delta\mu$, the B-dependent Coulomb charging, the Zeeman splitting, and the temperature:

$$\Delta\mu_s = E_{CB}(B) + 2k_BT \ln\left[2\cosh\left(\frac{|g|\mu_B B}{2k_BT}\right)\right]. \quad (1)$$

Figure 1(c) shows $\Delta\mu$ as a function of the magnetic field and the corresponding fit to Eq. (1) for the s shell at $\theta = \pi/2$ (i.e., in-plane magnetic field). For the p shell, the same description applies, and a similar relation can be derived. However, the observed addition energies and the dependence on $\mathbf{B}$ are smaller [Fig. 1(c)], and it becomes difficult to implement a reliable fit because of two additional factors: (i) a smaller Coulomb charging energy and (ii) broadening of the capacitance peaks due to the Coulomb disorder. Coulomb charging is given by $E_C^p = 3/4E_C^s$ while Coulomb disorder scales as n^2, where n is the

number of electrons trapped inside the QDs [22]. In order to fit the data, we assume $E_C^p(B) = E_C^p(0)$ and retained the temperature dependence [from Eq. (1)]. Although an approximation, it is instructive to present this analysis as it represents an upper bound on the g tensor, and, most importantly, it can help in elucidating the symmetries for this particular state. This reasonably simple model which takes into account the most important factors in determining the Zeeman splitting in quantum dots, including temperature effects and wave function compression, describes well the whole data set.

From the g factor obtained at each angle and for each shell, the g-tensor modulus was determined for the polar and azimuthal scans by $|g_{\mathrm{pol}}| = \sqrt{g_{[001]}^2 \cos(\theta)^2 + g_{[110]}^2 \sin(\theta)^2}$ and $|g_{\mathrm{az}}| = \sqrt{g_{[110]}^2 \cos(\phi)^2 + g_{[1\bar{1}0]}^2 \sin(\phi)^2}$. Figures 2 and 3 show the polar and azimuthal scans. In the top panel, the experimental setup is represented showing the orientation of the magnetic field with respect to the QD crystalline axis, as well as the FD wave functions for each shell calculated for $\mathbf{B} = 15$ T. The data are shown in the bottom panel with corresponding fits.
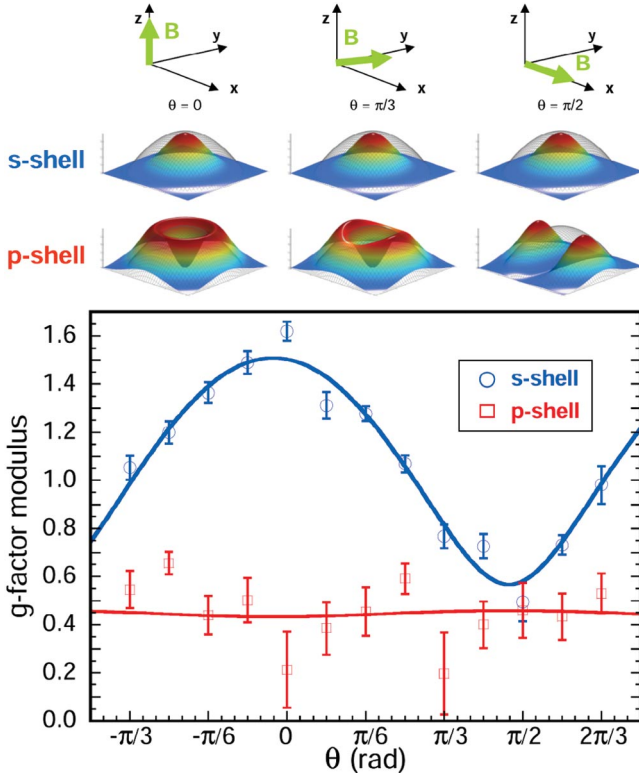
From the polar scan, one can immediately note that for the s shell the g factor is quite anisotropic, whereas for the p shell it is constant and always smaller. This is a quite surprising result at first, considering the single-particle energy ($\hbar\omega_0 = 37.8$ meV) and confinement along z ($E_z = -280$ meV) and the fact that the z component of the wave function for both states is basically the same. From the fit, we find $|g_{[001]}^s| = 1.51 \pm 0.03$ and $|g_{[110]}^s| = 0.57 \pm 0.05$, and $|g_{[001]}^p| \approx |g_{[110]}^p| = 0.47 \pm 0.07$. The larger values for g^s are consistent with a stronger localization inside the QD due to the deeper confinement. In order to draw a qualitative picture for the wave functions, we plot the solutions for the s and p wave functions for different magnetic-field tilt angles (Figs. 2 and 3, top panel). Insofar as the behavior for $|g^s|$ is concerned, one notes that the wave function is more localized into the QD and, consequently, more sensitive to the confinement potential details at the QD center. A high anisotropy is expected given the pancake geometry of the QDs. The somewhat unexpected result comes about for the p shell. A highly isotropic behavior is found, and we associate this behavior to the symmetry of the p wave function, as depicted in the upper panel in Fig. 2. First, as the electrons on the p shell are more delocalized, a leakage of the wave function along the growth direction takes place, which brings the g-factor modulus values

FIG. 2 (color).   (Top) Wave function for the s and p shells for three directions on the applied magnetic field $\theta = 0$, $\theta = \pi/3$, and $\theta = \pi/2$. x, y, and z correspond to the [110], [1$\bar{1}$0], and [001] directions, respectively; a QD is schematically represented in the same plot. (Bottom) g tensor for the s and p shells for the polar scan.
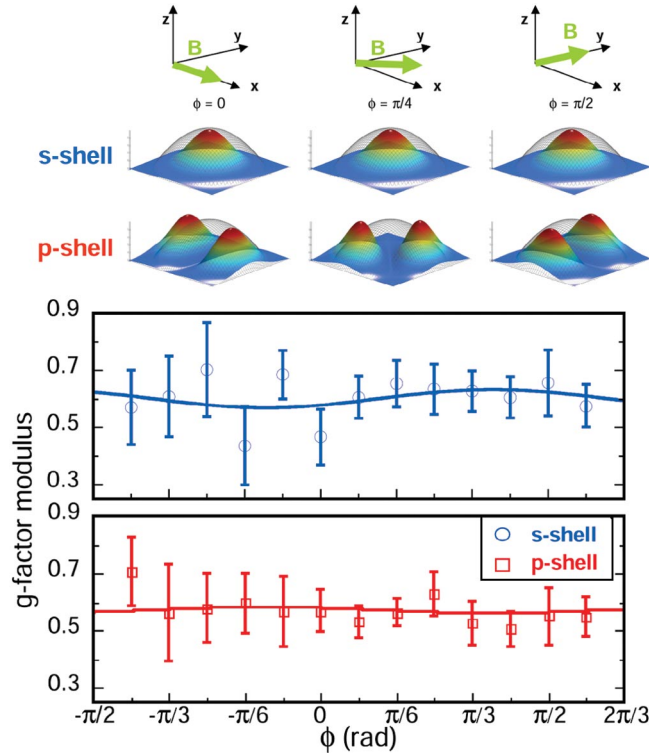

FIG. 3 (color).   (Top) Wave function for the s and p shells for three directions on the applied magnetic field $\phi = 0$, $\phi = \pi/4$, and $\phi = \pi/2$. x, y, and z correspond to the [110], [1$\bar{1}$0], and [001] directions, respectively; a QD is schematically represented in the same plot. (Bottom) g tensor for the s and p shells for the azimuthal scan.
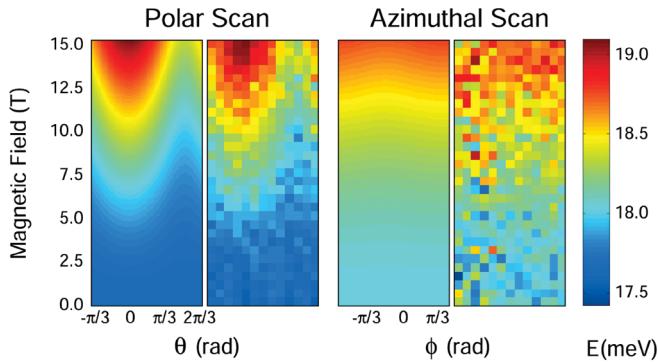
FIG. 4 (color). (Left) Calculated and measured addition energies for the polar scan; (right) same for the azimuthal scan.

closer to that of the matrix ($|g_{GaAs}| = 0.44$). Second, the wave function for the *p* shell has a node at the center of the QDs, which permits probing of the regions outside or at the interfaces of the QDs. Hence, by measuring the *g* factor for the *s* and *p* shells, one can evaluate the details of the confining potential at selected spatial locations, in a similar fashion that was carried out for the determination of the chemical environment of deep levels [7].

Figure 3 shows the *g* tensor for an in-plane field configuration (azimuthal scan). For both *s* and *p* shells, the *g* factor is independent of the field direction within the experimental uncertainties, consistent with a cylindrical symmetry for the QDs.

Several competing effects have to be taken into account when interpreting the obtained results: (i) local strain and local crystal fields which change the details of the confining potential, (ii) nonuniform composition, (iii) quantum confinement, and (iv) nonparabolicity, which takes place in InAs. All of these parameters may influence the spin-orbit coupling, which is one of the important components in the *g*-factor determination. Modifications into the *g* factor have been demonstrated by tuning both strain [20,23] and composition [24] in the QDs. If one compares these experimental results with theory, a good agreement is found which corroborates the description by Pryor *et al.* [21]. In essence, we find that effects (i)–(iii) are basically the same, and they by and large determine the behavior for the *g* tensor. More careful experiments on different samples are required to draw a more complete picture on the relative effect of each component.

As a final verification of the models utilized in this work, we calculate the electron addition energy for $n = 2$, i.e., *s*-shell filling, from the values obtained from the fits. The addition energy can be calculated according to Eq. (1). Figure 4 shows the calculated (left) and measured (right) results for the polar and azimuthal scans. This comparison is useful in evaluating the adequacy of the proposed model, the signal to noise ratio, and an overall picture of what can be resolved for this two electron system. An important

point mentioned previously was that of ensemble measurements. In this experiment, one obtains a more reliable evaluation of the *g* tensor as one is averaging over many different spin configurations which are temperature- and magnetic-field-dependent. This experiment thus provides a more representative description of the *g* tensor in nanostructures.

In summary, we have inferred the *g* tensor for the *s* and *p* shells of self-assembled QDs. We found that for the *s* shell the *g* tensor is highly anisotropic, reflecting the confinement potential details. For the in-plane component and for the *p* shell, the moduli of the inferred *g* factors were close to the bulk GaAs value. Finally, we found that for the *p* shell the *g* tensor was isotropic within our experimental resolution, which is consistent with the wave function having a node at the QD center and being more delocalized along the growth direction.

*Corresponding author.
Electronic address: gmedeiros@lnls.br
[1] S. A. Wolf *et al.*, Science **294**, 1488 (2001).
[2] D. Loss *et al.*, Phys. Rev. A **57**, 120 (1998).
[3] L. M. Roth *et al.*, Phys. Rev. **114**, 90 (1959).
[4] R. J. Elliot, Phys. Rev. **96**, 266 (1954).
[5] For example, C. Weisbuch and C. Hermann, Phys. Rev. B **15**, 816 (1977).
[6] *Electron Paramagnetic Resonance of Transition Ions*, edited by A. Abragam (Clarendon, Oxford, 1970).
[7] F. G. Anderson *et al.*, Phys. Rev. B **45**, 3279 (1992).
[8] L. M. Roth, Phys. Rev. **118**, 1534 (1960).
[9] C. Calero *et al.*, Phys. Rev. Lett. **95**, 166603 (2005).
[10] A. Malinowski *et al.*, Phys. Rev. B **62**, 2051 (2000).
[11] M. Oestreich *et al.*, Europhys. Lett. **31**, 399 (1995).
[12] J. R. Petta and D. C. Ralph, Phys. Rev. Lett. **89**, 156802 (2002); **87**, 266801 (2001).
[13] S. Lindemann *et al.*, Phys. Rev. B **66**, 195314 (2002).
[14] R. Hanson *et al.*, Phys. Rev. Lett. **91**, 196802 (2003).
[15] R. J. Warburton *et al.*, Phys. Rev. B **58**, 16 221 (1998).
[16] Lixin He and Alex Zunger, Phys. Rev. B **73**, 115324 (2006).
[17] M. Bayer *et al.*, Phys. Rev. Lett. **82**, 1748 (1999).
[18] A. R. Goñi *et al.*, Jpn. J. Appl. Phys. **39**, 3907 (2000).
[19] G. Medeiros-Ribeiro *et al.*, Appl. Phys. Lett. **80**, 4229 (2002).
[20] G. Medeiros-Ribeiro *et al.*, Appl. Phys. A **77**, 725 (2003).
[21] C. E. Pryor *et al.*, Phys. Rev. Lett. **96**, 026804 (2006).
[22] G. Medeiros-Ribeiro *et al.*, Phys. Rev. B **55**, 1568 (1997).
[23] T. Nakaoka *et al.*, Phys. Rev. B **71**, 205301 (2005).
[24] M. T. Björk *et al.*, Phys. Rev. B **72**, 201307(R) (2005).